Research Square

Preprints are preliminary reports that have not undergone peer review.
They should not be considered conclusive, used to inform clinical practice,
or referenced by the media as validated information.

Cryo-EM structures of human α-synuclein filaments reveal the molecular basis of PET tracer ACI-12589 recognition

Yang Yang

yang.yang@vai.org

Van Andel Research Institute https://orcid.org/0000-0003-2238-6437

Katelyn Ernst

Van Andel Research Institute

Hongwei Zhang

Van Andel Research Institute

Francesca Capotosti

AC Immune

Patrick Cullinane

UCL Queen Square Institute of Neurology

Henry Houlden

UCL Queen Square Institute of Neurology and The National Hospital for Neurology and Neurosurgery
https://orcid.org/0000-0002-2866-7777

Huw Morris

UCL Queen Square Institute of Neurology

Airi Tarutani

Tokyo Metropolitan Institute of Medical Science

Kazuko Hasegawa

National Hospital Organization Sagamihara National Hospital

Masato Hasegawa

Tokyo Metropolitan Institute of Medical Science

Zane Jaunmuktane

UCL Queen Square Institute of Neurology

Article

Keywords:

Posted Date: November 11th, 2026

DOI: https://doi.org/10.21203/rs.3.rs-11652509/v1

License: This work is licensed under a Creative Commons Attribution 4.0 International License.
Read Full License

Additional Declarations: There is **NO** Competing Interest.

Cryo-EM structures of human α-synuclein filaments reveal the molecular basis of PET tracer ACI-12589 recognition

Katelyn Ernst[1,2*], Hongwei Zhang[1*], Francesca Capotosti[3], Patrick W. Cullinane[4,5,6], Henry Houlden[4], Huw Morris[7], Airi Tarutani[8], Kazuko Hasegawa[9], Masato Hasegawa[8], Zane Jaunmuktane[4,5,10], Yang Yang[1,2 #]

[1] Department of Structural Biology, Van Andel Institute, Grand Rapids, MI, USA

[2] Van Andel Institute Graduate School, Grand Rapids, MI, USA

[3] AC Immune SA, EPFL Innovation Park, Building B, 1015, Lausanne, Switzerland

[4] Department of Clinical and Movement Neurosciences, UCL Queen Square Institute of Neurology, London, UK

[5] Queen Square Brain Bank for Neurological Disorders, UCL Queen Square Institute of Neurology, London, UK

[6] Queen Square Movement Disorders Centre, UCL Queen Square Institute of Neurology, London, UK

[7] Department of Neuromuscular Diseases, UCL Queen Square Institute of Neurology, London, UK

[8] Department of Clinical Medical Sciences, Tokyo Metropolitan Institute of Medical Science, Tokyo, Japan

[9] Division of Neurology, National Hospital Organization Sagamihara National Hospital, Sagamihara, Kanagawa, Japan

[10] Division of Neuropathology, National Hospital for Neurology and Neurosurgery, University College London NHS Foundation Trust, London, UK

* Equal contributions

[#] Correspondence: yang.yang@vai.org (Y.Y.)

Abstract

Misfolded α-synuclein adopts distinct amyloid architectures across synucleinopathies, complicating the development of PET tracers for *in vivo* detection. Here, we used cryo-EM to determine how the clinically evaluated tracer ACI-12589 recognizes disease-derived α-synuclein filaments isolated from human brain. In MSA type I and II filaments, ACI-12589 occupies a conserved C-terminal cleft in protofilament A, forming a diagonal array stabilized by hydrogen bonds and cooperative aromatic stacking without detectable backbone rearrangement. Recognition of PD filaments was strongly architecture dependent: no ordered ligand density was observed in singlet Lewy folds from idiopathic PD or *SNCA* H50Q-associated PD, whereas ACI-12589 bound an exposed β-sheet surface in the G51D dimerised Lewy fold in a geometry distinct from that observed in MSA. These structures reveal the molecular basis of fold-dependent tracer recognition and provide a framework for interpreting variable imaging signals and developing next-generation α-synuclein PET agents.

Introduction

The abnormal accumulation of misfolded α-synuclein proteins in the brain is a hallmark of a group of neurodegenerative disorders collectively known as synucleinopathies[1, 2], including Parkinson's disease (PD), dementia with Lewy bodies (DLB), and multiple system atrophy (MSA). Increasing evidence indicates that assembled α-synuclein propagates through templated seeding mechanisms, driving the spread of pathology and neurodegeneration [3]. Although these disorders share α-synuclein aggregation as a common pathological feature, they exhibit distinct clinical manifestations, cellular vulnerabilities, and patterns of regional brain involvement. In PD and DLB, α-synuclein predominantly accumulates within neuronal Lewy bodies and Lewy neurites, whereas MSA is characterized by abundant oligodendroglial cytoplasmic inclusions together with intracellular neuronal aggregates [3-6]. Our previous cryo-EM studies have shown that α-synuclein filaments from idiopathic PD and DLB adopt a single protofilament architecture termed the Lewy fold[7 8], whereas disease-associated A53T and G51D mutations can give rise to a dimerised Lewy fold [9]. G51D is particularly notable because it causes familial parkinsonism with clinicopathological features that overlap with MSA[10, 11], whereas the association of H50Q with familial PD has been less consistent[12]. By contrast, MSA α-synuclein filaments contain two main structural types, designated types I and II, each composed of two non-identical protofilaments (PF-A and PF-B) arranged in an asymmetric cross-β architecture [13]. A further subtype of type I filaments was characterized with a slight change in protofilament A [14]. Although PF-A and PF-B share some β-strand motifs, they differ in side-chain packing and inter-protofilament contacts, producing distinct molecular surfaces and grooves that are absent in Lewy fold filaments. These disease-associated filament folds generate distinct molecular surfaces and intermolecular interfaces that are likely to influence both pathogenic propagation and molecular recognition.

Positron emission tomography (PET) imaging provides a powerful, non-invasive approach to detect and monitor protein aggregation *in vivo,* making it a valuable tool for disease diagnosis as well as progression tracking [15-18]. PET tracers targeting amyloid-β plaques and tau neurofilamental tangles are now widely used in Alzheimer's disease [17,

[19-21], whereas the development of α-synuclein tracers has proven substantially more challenging owing to the relatively low abundance, structural heterogeneity, and conformational diversity of α-synuclein aggregates [5, 22, 23]. Cryo-EM has been used to elucidate the binding mechanisms of small molecules and PET tracers to amyloid filaments, providing structural insights into how ligands recognize amyloids [24, 25]. These studies have determined binding to tau paired helical filaments [26-28], chronic traumatic encephalopathy tau filaments [29], *in vitro* assembled α-synuclein filaments [22, 23, 25, 30] and TMEM106B filaments [31]. These structures explain the high affinity and selectivity of existing PET tracers and show that differences in filament conformation create distinct binding environments that likely contribute to variability in imaging signals between diseases and across patients. Recent α-synuclein PET tracers, including [^{18}F] ACI-12589 and [^{11}C] MODAG-005, have entered early clinical evaluation, but their binding profiles differ across synucleinopathies [32 33]. However, no structure has yet revealed how an imaging ligand engages disease-derived α-synuclein filaments isolated from human brain tissue.

[^{18}F] ACI-12589 is a clinically evaluated PET tracer that has been designed to bind to pathological α-synuclein aggregates, while being selective over other amyloid filaments, such as amyloid beta, tau and TDP-43. Indeed, *in vitro,* autoradiography experiments showed strong binding of [^{18}F] ACI-12589 to α-synuclein inclusions in postmortem in different synucleinopathy tissues, with minimal off-target binding to amyloid-β, tau, or myelin-rich regions [34]. In clinical testing, [^{18}F] ACI-12589 was found to distinguish MSA from other kinds of neurodegenerative diseases as well as to distinguish MSA subtypes based on the PET signal uptake in different brain areas. Particularly, first-in-human PET imaging with [^{18}F] ACI-12589 demonstrated high retention in MSA-affected brain regions, including cerebellar white matter and middle cerebellar peduncles, in MSA subtypes C and P respectively, but negligible binding in PD, DLB, or control subjects. Interestingly preclinical data, using high resolution autoradiography or radiobinding assays in human brain tissue, revealed that [^{18}F] ACI-12589 is not exclusively MSA-specific, displaying high affinity for α-synuclein aggregates from sporadic and familial (e.g. G51D mutation carrier) parkinsonism cases as well as DLB cases. These findings indicate that ACI-12589 is not specific to a single disease and instead may interact differentially

with distinct α-synuclein assemblies. The structural basis of these differences has remained unknown.

Here, we used cryo-EM to investigate ACI-12589 binding to human brain-derived α-synuclein filaments encompassing distinct architectures associated with MSA and PD. In addition to MSA type I and type II filaments, we examined two independent samples containing the singlet Lewy fold, from idiopathic PD and H50Q-associated PD, as well as the dimerized Lewy fold associated with the *SNCA* G51D mutation. ACI-12589 bound a conserved C-terminal cleft in both MSA filament types and a distinct exposed β-sheet surface in the G51D dimerised Lewy fold, whereas no ordered ligand density was detected in either singlet Lewy fold. These findings demonstrate that ACI-12589 binding is architecture-dependent and define the molecular environments compatible with ordered tracer binding.

Results

ACI-12589 binds a C-terminal cleft in two types of MSA α-synuclein filaments

To better characterize the molecular basis of ACI-12589 recognition, we performed cryo-EM structure determination of two types of α-synuclein filaments from two neuropathologically confirmed cases of MSA following incubation with ACI-12589 (Supplementary Table 1). Sarkosyl-insoluble α-synuclein filaments extracted from the putamen of case 1 and frontal cortex of case 2 were incubated with ACI-12589 (Fig. 1a) at room temperature. α-synuclein filaments from case 1 were predominantly of MSA type I, whereas filaments from case 2 were exclusively of type II. Helical reconstruction in RELION yielded maps of MSA type I and type II filaments at resolutions of 2.7Å and 2.6Å, respectively (Fig. 1b, 1c, Extended Data Fig. 1 and Supplementary Table 2). Comparison with previously reported structures of MSA type I and type II filaments (PDB codes: 6XYO and 9CX6) revealed an additional density in a V-shaped cavity at the C-terminus of protofilament A in both filament types. We calculated difference maps between our reconstructions and the reference maps using EMDA [35], with green colored densities indicating the extra densities from the ACI-12598-incubated maps. After resampling and aligning the maps to the same grid and coordinate frame, subtraction at 3.0 Å resolution revealed extra densities along the protofilament interface (Fig. 1c and 1e)[13]. The main

difference between the maps with and without the PET tracer is an additional density in the V-shaped cavity of the C-terminus in protofilament A from both filament types, which extends up to 16 standard deviations above the mean, suggesting that they arise uniquely from the incubation with ACI-12589 (Fig. 1d-1g). The absence of other difference densities across the filament suggests a single, specific binding site for ACI-12589. Additional, poorly resolved non-proteinaceous densities[36] that have previously been attributed to unknown cofactors [13] are present in maps with or without PET tracer.

A diagonal ligand array stabilizes ACI-12589 binding to MSA α-synuclein filaments

ACI-12589 binds to both type I and type II MSA α-synuclein filaments with a single ligand molecule for each β-rung of the amyloid filament (Fig. 2). Superposition of the refined atomic models with ligands to those without showed minimal deviations in the α-synuclein molecules, with root mean-square deviations *(r.m.s.d)* less than 1Å, confirming that PET tracer binding is localized and does not perturb the overall filament architecture (Extended Data Fig. 2). The ligand ACI-12589 occupies a V-shaped cleft at the C-terminus of protofilament A, where the pyridine moiety is buried in the cavity (Fig. 2a and 2e). To determine the pose, we first placed ACI-12589 into the extra density and explored chemically reasonable torsions. Aromatic rings were kept planar; and torsions about the pyridinyl–linker and linker–aryl single bonds were sampled. Two global orientations were evaluated: with the pyrrolidine ring facing toward the filament core versus facing outward. The inward-facing orientation produced steric clashes with nearby protein atoms. The selected outward-facing orientation eliminated clashes, maximized real-space map–model correlation, and positioned the aromatic system to make favorable π contacts (stacking/edge-to-face) with hydrophobic side chains lining the pocket. In both type I and type II filaments, ACI-12589 binding is further anchored by two hydrogen bonds from the ligand to S87 and T92 with distance of 2.67 Å and 3.15 Å for Type I (Fig. 2b) and 2.80 Å and 2.64 Å for Type II (Fig. 2f).

Along the helical axis, the ACI-12589 adopts a diagonal orientation following the helical symmetry of the amyloid fold. Each ACI-12589 molecule binds one α-synuclein subunit per helical layer, and binding is further stabilized by aromatic stacking interactions (Fig. 2d and 2h). While the distance from ligand to ligand on the filament axis is consistent

with helical rise (~4.8Å), the angle between the plane of ligand molecule and α-synuclein protein is about 45 degrees (Fig. 2 c, d, g and h). This angle of ligand binding shifted the planes of the aromatic rings to a parallel offset pattern, resulting in a distance between molecules at a favorable distance for π–π stacking (with a 3.5 Å inter-plane distance; Fig. 2d and 2h). Another π interaction that further stabilizes binding is between the aromatic rings in ACI-12589 and that of the F94 side chains. The edge-to-face orientation of aromatic rings results in T-shaped π stacking, with the positively charged framework of one ring interacting with the π electron cloud of the side chain ring. Together, these contacts create a cooperative binding arrangement that stabilizes ACI-12589 along the filament surface.

ACI-12589 binding differs between singlet and dimerised Lewy folds

To further investigate ACI-12589 binding to Lewy fold architectures, we examined α-synuclein filaments from idiopathic PD and from PD cases carrying heterozygous *SNCA* H50Q or G51D mutations. α-synuclein filaments from idiopathic PD and H50Q PD adopt the singlet Lewy fold and contain the additional density termed Island A, whereas G51D filaments adopt a dimerised Lewy fold in which Island A is absent (Supplementary Table 2) [9]. Thus, the idiopathic PD and H50Q cases provided two independent examples of the singlet Lewy fold, whereas G51D provided a structurally distinct dimerized Lewy fold. G51D was of particular interest because previous autoradiography and radiobinding studies showed prominent ACI-12589 binding to α-synuclein aggregates from this case[34]. Following incubation with ACI-12589, cryo-EM structures of the idiopathic PD, H50Q, and G51D filaments were determined at resolutions of 2.8 Å, 3.3 Å, and 3.0 Å, respectively (Fig. 3, Extended Data Fig. 3, Extended Data Fig. 4 and Supplementary Table 2). Comparison of the ACI-12589-incubated idiopathic PD and H50Q maps with their corresponding ligand-free structures revealed no additional ordered density attributable to ACI-12589 (Fig. 3a, 3c, and Extended Data Fig. 4). Thus, under the conditions examined, no well-ordered ACI-12589 binding site was resolved in either example of the singlet Lewy fold.

By contrast, the ACI-12589-incubated G51D filaments displayed additional density that was absent from the corresponding ligand-free structure (Fig. 3b, 3d and 3g). This density

is located along an exposed β-sheet surface of the filament core between residues D51 and E57 (Fig. 3e and 3f). Unlike the diagonal arrangement of ACI-12589 in MSA filaments, the ligand density in G51D runs approximately parallel to the β-sheet and rung, following the helical symmetry of rise and twist as the core filament. Because the density did not permit unambiguous determination of ligand directionality, a plausible binding pose was modeled based on density agreement, steric compatibility and potential hydrophobic interactions.

Structural comparison of the singlet and dimerised Lewy fold showed that the ACI-12589-binding region exposed in G51D corresponds to a region occupied by Island A singlet Lewy fold. The presence of Island A in both idiopathic PD and H50Q filaments may therefore reduce accessibility to this surface, whereas its absence in the G51D assembly creates an exposed region compatible with ordered ACI-12589 binding. Other structural differences between the singlet and dimerised Lewy folds may also contribute to the observed differences in ligand binding.

Conserved binding compatibility of ACI-12589 across MSA Type I and Type II α-synuclein filament

To assess whether this binding mode is preserved across MSA polymorphs, we compared currently available human MSA filament structures, including type I (PDB 6XYO), type I_2 (PDB 9CDA), type II_1 (PDB 6XYP and 9CX6), and type II_2 (PDB 6XYQ) filaments. MSA type III was not compared here because it adopts a substantially different filament architecture. Structural comparisons showed that the C terminus cleft of protofilament A is highly conserved across the four type I and type II subtypes examined (Fig. 4a-4d). The two type I subtypes have closely related protofilament A structures surrounding the binding site and generate nearly identical C-terminal cavities. In type II subtypes, structural variation is concentrated primarily in protofilament B, whereas the local geometry of the protofilament A binding cleft is retained. In all four subtypes, S87 and T92 are oriented toward the cavity and are positioned to support hydrogen bonding with ACI-12589, while F94 projects toward the ligand-binding region and can support aromatic interactions. Electrostatic interactions indicate the hydrogen bonding and hydrophobic interactions that define this cavity (Extended Data Fig. 5).

Although the corresponding region of protofilament B is structurally similar to protofilament A, it contains an additional density that partially occludes the cavity, providing a possible explanation for the restriction of resolved ACI-12589 binding to protofilament A only (Fig. 4a and 4c). These comparisons indicate that the ACI-12589-binding pocket is a conserved structural feature of protofilament A in type I and type II MSA filaments and is compatible with ligand binding across these MSA filament subtypes.

ACI-12589 adopts distinct binding geometries in disease-derived α-synuclein filaments

Comparison of the MSA and G51D structures reveals two distinct modes of ACI-12589 binding. In MSA type I and type II filaments, the ligand occupies a recessed C-terminal cavity in protofilament A and forms a diagonal array stabilized by ligand–ligand stacking. In the G51D dimerized Lewy fold, ACI-12589 instead associates with an exposed β-sheet surface in an approximately parallel orientation. Related geometries have been observed for other small molecules bound to α-synuclein filaments. A similar diagonal arrangement has been observed for CNS-11g [37] bound to MSA type I α-synuclein filaments (PDB 9E8W), suggesting that the C-terminal cleft of protofilament A can accommodate chemically distinct ligands through a related binding geometry (Fig. 4e). In the G51D dimerised Lewy fold, ACI-12589 binds along an exposed β-sheet surface in an orientation approximately parallel to the filament axis (Fig. 4f). A parallel binding arrangement has also been reported for FD4 bound to a singlet Lewy fold structure (PDB 9V6U), and occupy a similar region of the α-synuclein sequence and local filament surface (Fig. 4g and 4h). These comparisons show that disease-derived α-synuclein filaments can accommodate small molecules through two distinct structural environments and ligand geometries (Fig. 4f and 4i). ACI-12589 therefore does not recognize a single conserved pocket across α-synuclein folds, but instead engages compatible sites depending on the combination of pocket shape, surface exposure, and filament architecture.

Discussion

The development of PET tracers for α-synuclein has remained considerably more challenging than for amyloid-β or tau, owing to the relatively low abundance of

pathological α-synuclein aggregates, their intracellular localization, and the remarkable structural heterogeneity of disease-associated filaments. A recent autoradiographic comparison of ACI-12589 and asyn-44 reported tracer-specific binding differences between MSA and PD tissues, as well as possible off-target binding of ACI-12589 to amyloid-β plaques[38], further emphasizing the need to define the structural environments that support ligand recognition. Here, we present cryo-EM structures of the clinically evaluated PET tracer ACI-12589 bound to disease-derived α-synuclein filaments extracted directly from human brain. The structures show that ACI-12589 is accommodated by distinct molecular environments in different disease-associated α-synuclein filament folds. In MSA filaments, the tracer binds a conserved C-terminal cavity in protofilament A, whereas in the G51D dimerized Lewy fold it associates with an exposed β-sheet surface through a different binding geometry. By contrast, no ordered ligand density was resolved in two independent examples of the singlet Lewy fold, from idiopathic PD and H50Q PD. Together, these findings provide a structural framework for understanding how the same PET ligand interacts with structurally diverse α-synuclein assemblies.

Comparison with other α-synuclein PET ligand structures suggests emerging principles of amyloid molecular recognition. The PET ligand F0502B[22], together with more recent structures of CNS-11g (PDB 9E8W) and FD4 (PDB 9V6U), established that small molecules can bind defined sites on human α-synuclein filaments. Our structures extend these observations by demonstrating that the same ligand can adopt distinct binding modes on different disease-derived filament architectures. ACI-12589 and CNS-11g bind MSA filaments through a diagonal arrangement within a C-terminal cavity, whereas ACI-12589 in the G51D dimerized Lewy fold and FD4 in Lewy fold filaments adopt a binding mode that is approximately parallel to the filament axis. Despite these differences, all currently available α-synuclein ligand structures share one notable feature: ligand molecules are organized according to the helical symmetry of the underlying amyloid filament. Rather than binding randomly to the filament surface, PET ligands appear to assemble into periodic arrays dictated by the repeating architecture of the filament. The available structures therefore suggest two complementary features of amyloid ligand recognition: a locally compatible molecular environment defined by pocket geometry and

side-chain organization, and a ligand arrangement compatible with the repeating helical architecture of the filament.

The comparison between singlet and dimerized Lewy folds further illustrates the importance of local site accessibility. The absence of ordered ACI-12589 density in both idiopathic PD and H50Q filaments argues against the H50Q substitution itself being responsible for the lack of a resolved binding site. Instead, the ACI-12589-binding region exposed in the G51D dimerized Lewy fold corresponds to a region occupied by Island A in both singlet Lewy-fold structures. This suggests that the presence of Island A may reduce accessibility to this surface, whereas its absence in G51D permits ordered ligand accommodation. Other differences between the singlet and dimerized Lewy folds, including protofilament organization, local side-chain packing and surface properties, may also contribute. Notably, the G51D mutation is associated with familial parkinsonism showing some clinicopathological features that overlap with MSA, yet its α-synuclein filaments adopt a dimerized Lewy fold rather than an MSA fold. The ability of ACI-12589 to bind both assemblies therefore illustrates that ligand-compatible environments can arise in structurally distinct disease-associated α-synuclein folds.

Our findings also highlight the importance of studying ligand interactions using disease-derived filaments. Although several recombinant α-synuclein filaments adopt overall folds resembling those observed in human brain, structural similarity alone does not predict ligand recognition. Notably, a recently deposited cryo-EM structure of ACI-12589 incubated with an *in vitro* assembled α-synuclein filament (PDB 9KCP) does not show ordered ligand density despite apparent similarities in filament architecture. Likewise, α-synuclein filaments assembled in mouse brain (PDB 9RZF) [39] differ substantially from human disease-derived structures (Extended Data Fig. 6). These observations suggest that ligand recognition depends on features extending beyond the protein backbone, including local side-chain conformations, filament folding, post-translational modifications, electrostatic environment, and associated non-proteinaceous components [40].

The structural differences observed here also provide a framework for interpreting the heterogeneous imaging behavior of ACI-12589 across synucleinopathies. While *ex-vivo*, ACI-12589 binds broadly to different forms of α-synuclein aggregates, clinical PET

imaging demonstrates robust tracer retention in MSA lower but detectable signals in a familial form of PD (*SNCA* duplication carriers), but no relevant signal in sporadic PD or DLB cases. Our structures suggest that these differences arise, at least in part, from the compatibility of individual filament architectures with ACI-12589 binding. However, filament structure is unlikely to be the only determinant of PET signal. Compared with amyloid-β plaques or tau neurofibrillary tangles, the overall burden of aggregated α-synuclein in PD is relatively low, and Lewy pathology is predominantly intracellular and regionally heterogeneous. Consequently, even ligands capable of recognizing Lewy filament conformations may produce limited *in vivo* contrast because of the relatively small number of accessible binding sites. Variation in aggregate abundance, filament composition, and regional pathology therefore probably contributes together with structural compatibility to the PET signals observed in patients.

While the structures presented here establish the molecular basis of ACI-12589 binding to several disease-derived α-synuclein filament architectures, additional filament conformations from human synucleinopathies remain to be investigated. Future structural studies will be important to determine whether the architecture-dependent binding principles identified here extend across the broader spectrum of α-synuclein polymorphs. Combining cryo-EM with quantitative binding measurements, autoradiography, and *in vivo* PET imaging will further help relate atomic binding mechanisms to tracer performance in human disease.

Our structures provide a molecular framework for interpreting how PET ligands interact with disease-derived human α-synuclein filaments. Rather than recognizing a universal structural motif, ACI-12589 binds compatible molecular environments generated by distinct disease-associated filament architectures. Together with recently reported α-synuclein ligand structures, our findings support a model in which ligand recognition emerges from the interplay between local binding-site chemistry, filament architecture, and the repeating helical symmetry of the amyloid assembly. We anticipate that integrating structural biology with molecular imaging will accelerate the rational development of next-generation tracers for the diagnosis and monitoring of synucleinopathies.

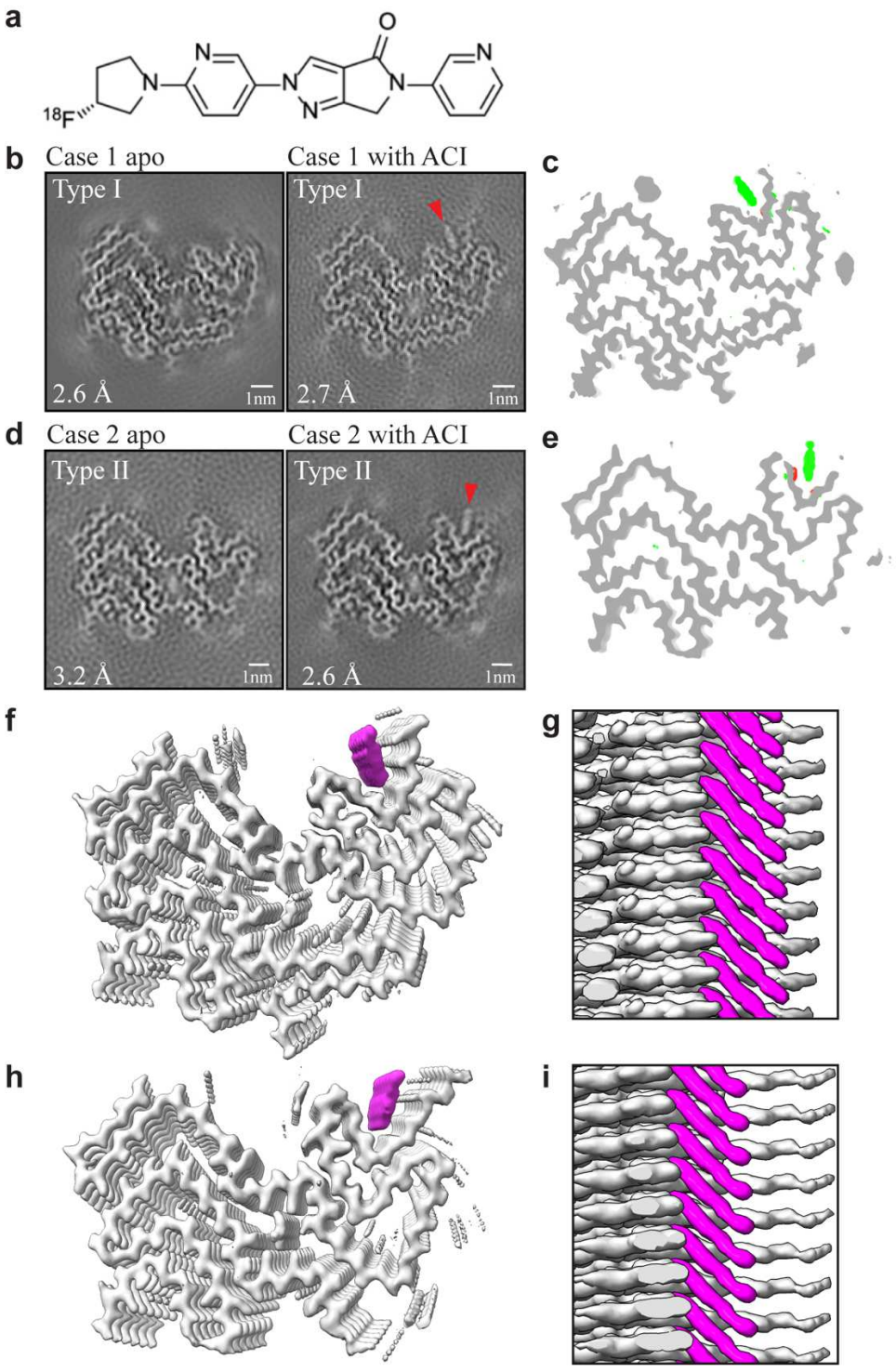


Fig. 1 | Cryo-EM maps of type I and type II MSA α-synuclein filaments with ACI-12589. **a,** Chemical structure of ACI-12589. **b,** Cryo-EM maps of type I filaments without (Case 1 apo) and with (Case 1 with ACI-12589) PET tracer. Scales, 1nm. Red arrows indicate the PET tracer densities. **c,** Difference maps for the of MSA type I filaments with

and without ACI-12589. Positive difference density is shown in green at a threshold of 12 standard deviations in the difference map; negative difference density is shown in red at a threshold of 12 standard deviations. **d,** Cryo-EM maps of type II filaments without (Case 2 apo) and with (Case 2 with ACI) PET tracer. **e,** Difference maps for the of MSA type II filaments with and without ACI-12589. Positive difference density is shown in green at a threshold of 9 standard deviations in the difference map; negative difference density is shown in red at a threshold of 9 standard deviations. **f** and **g,** Top and side view of cryo-EM map of type I filaments with ACI-12589. The density for ACI-12589 is colored in magenta. **h** and **I,** Top and side view of cryo-EM map of type II filaments with ACI-12589.

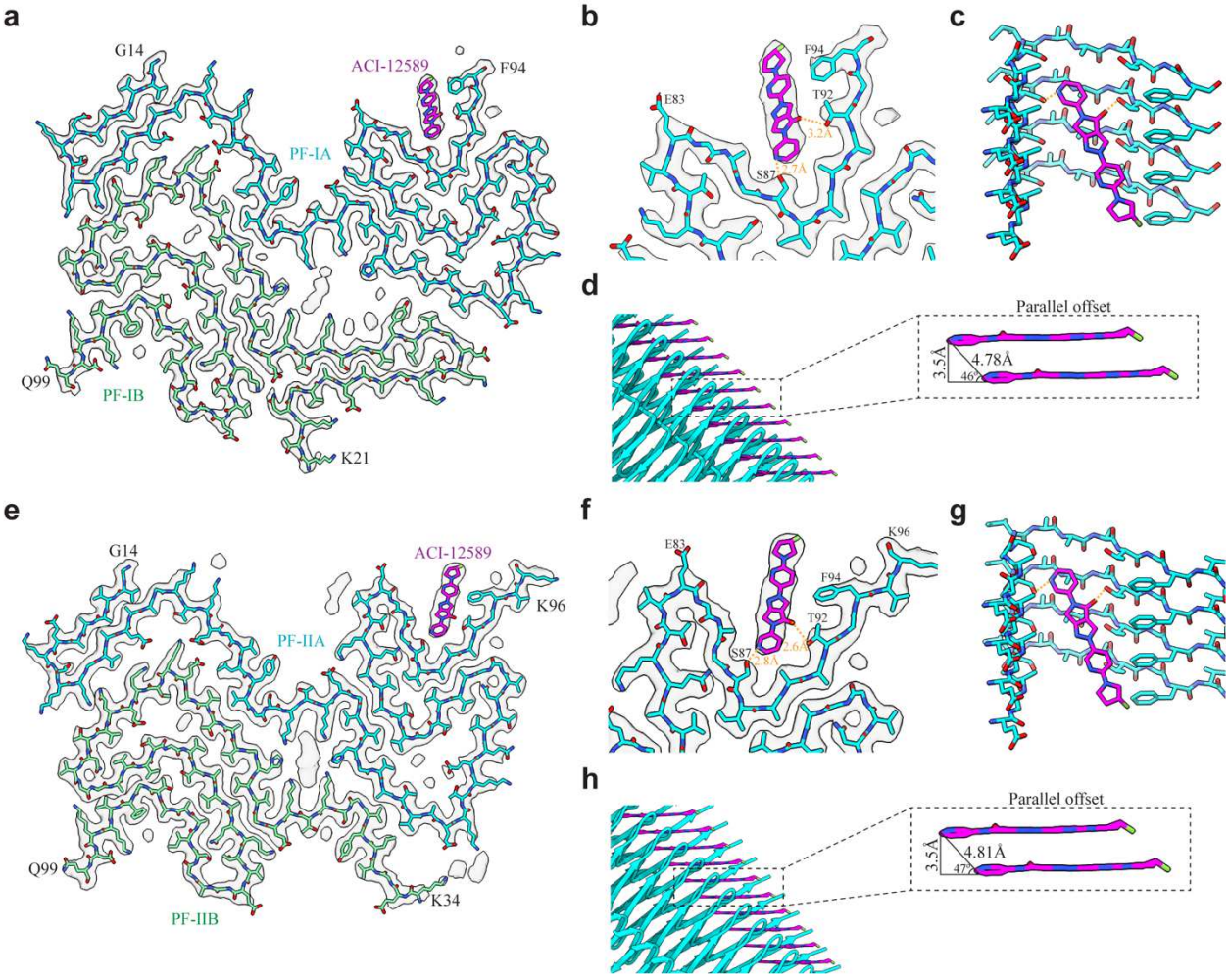


Fig. 2 | Binding architectures of type I and type II MSA filaments with ACI-12589. a, Cryo-EM electron density map and atomic model of type I filaments. The cryo-EM map (white) overlaid with the atomic model (protein in cyan, ACI-12589 in magenta). **b,** Close-up depiction of binding site and close contacts within type I filament binding cleft. **c,** Side view of one molecule of ACI-12589 within multiple layers of the type I filament binding pocket. **d,** Parallel offset of stacked ACI-12589 molecules with respect to the type I filament axis. **e,** Cryo-EM electron density map and atomic model of type II filaments. The cryo-EM map (white) overlaid with the atomic model (protein in cyan, ligand in magenta). **f,** Close-up depiction of binding site and close contacts within type II filament binding cleft. **g,** Side view of one molecule of ACI-12589 within multiple layers of the type II filament binding pocket. **h,** Parallel offset of stacked ACI-12589 molecules with respect to the type II filament axis.

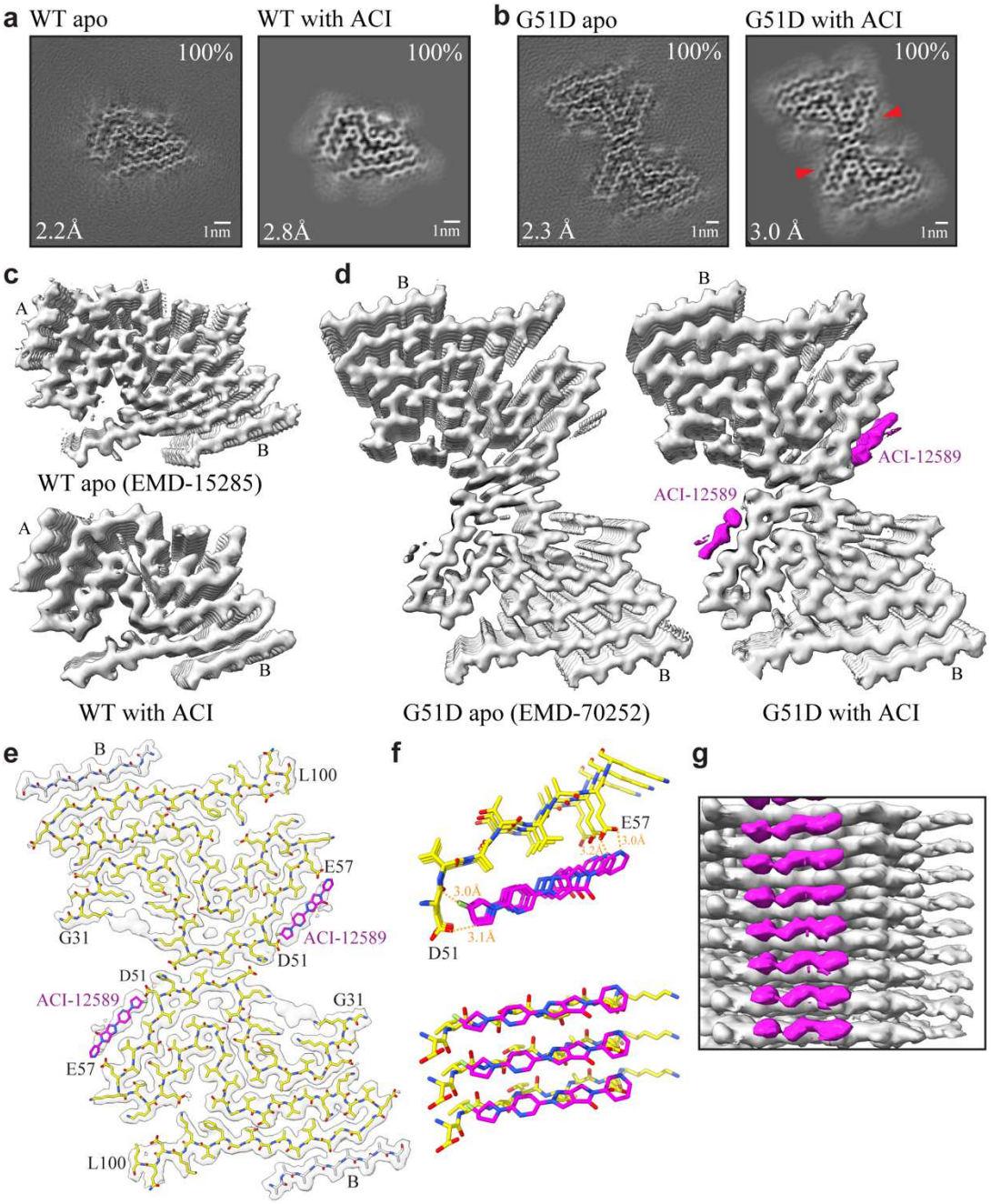


Fig. 3 | Cryo-EM structures of WT and G51D α-synuclein filaments following incubation with ACI-12589.

a and **b,** Cryo-EM maps of WT (A) and G51D (B) filaments without and with ACI-12589 PET tracer. Scales, 1nm. Red arrows in B indicate the additional density attributed to ACI-12589. **c,** Top view of cryo-EM maps of WT filaments without and with ACI-12589, showing no resolved additional ligand density. **d,** Top view of cryo-EM maps of G51D

filaments without and with ACI-12589. The additional density attributed to ACI-12589 is colored in magenta. **e,** Cryo-EM map and atomic model of the G51D filament with ACI-12589; ligand density is shown in magenta. **f,** Zoomed-in top and side views of the ACI-12589 binding site and ligand interactions. Hydrogen bonds are plotted with dashed lines. **g,** Side view of cryo-EM map of G51D filament with ACI-12589. The density for ACI-12589 is colored in magenta.

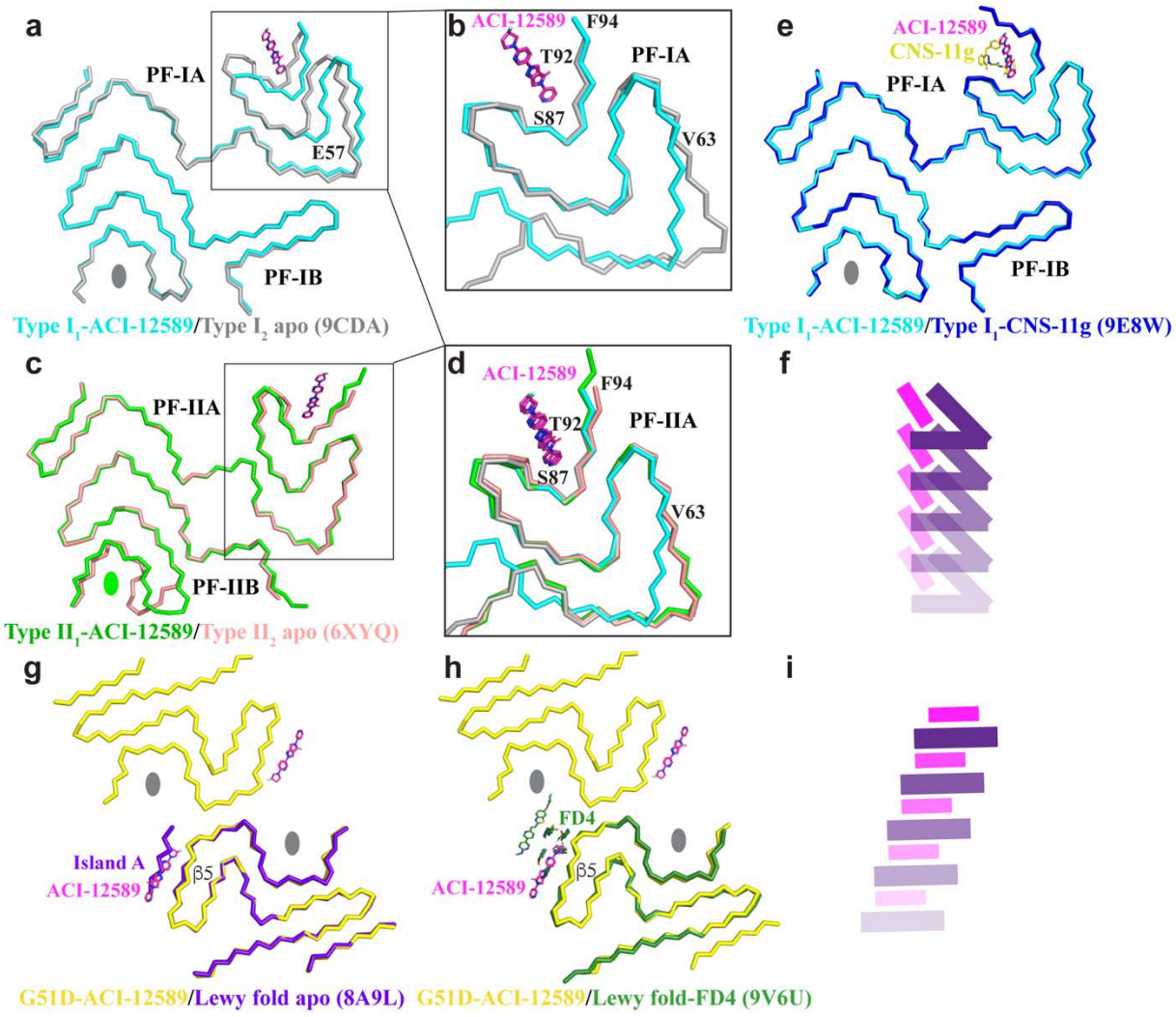


Fig. 4 | Distinct modes of ligand binding to disease-derived α-synuclein filaments.

a, Superposition of type I MSA filaments with ACI-12589. Type I_1 with ACI-12589 in cyan and type I_2 in gray. Protofilaments of PF-IA and PF-IB were indicated. Gray circles represent shared cofactors. **b,** Zoomed-in view of the superposition of type I C-termini. The superposition region starts from V63 to the end of C-terminus. **c,** Superposition of type II MSA filaments with ACI-12589. Type II_1 with ACI-12589 in green and type II_2 in salmon. Protofilaments PF-IIA and PF-IIB were indicated. Green circles represent cofactor in type II_1-ACI-12589. **d,** Zoomed-in view of the superposition of type I_1, type I_2, type II_1, and type II_2 C-terminus. **e,** Superposition of type I1 MSA filaments with ACI-12589 or CNS-11g. Type I_1 with ACI-12589 in cyan and type I_1 with CNS-11g in blue. Gray circles represent shared cofactors. **f,** Schematic representation of diagonal ligand-binding

geometry within the MSA filament pocket. Ligands are in pink and MSAs filaments in purple. **g,** Superposition of G51D filaments with ACI-12589 and WT filaments. G51D with ACI-12589 in yellow and WT in purple. Gray circles represent shared cofactors. **h,** Superposition of G51D filaments with ACI-12589 and Lewy fold with FD4. G51D with ACI-12589 in yellow and Lewy fold with FD4 in forest. Gray circles represent shared cofactors. **i,** Schematic representation of the approximately parallel ligand-binding geometry along the Lewy fold surface. Ligands are shown in pink and the filament in purple.

Methods

No statistical methods were used to predetermine sample size. The experiments were not randomized, and investigators were not blinded to allocation during experiments and outcome assessment.

Clinical history and neuropathology

Four postmortem brain samples were used in this study. Case 1 was an 85-year-old woman who died with a neuropathologically confirmed diagnosis of MSA-P following a 9-year history of bradykinesia, rigidity in upper and lower limbs and autonomic failure [13]. Case 2 developed short-term memory impairment and spatial disorientation at aged 58 and died at 66 with diagnosis of MSA but reviewed as an FTLD-synuclein case with MSA type II filaments, which was identified as MSA-FTLD subtype [41]. Case 3 was a female carrying a heterozygous *SNCA* H50Q mutation who developed PD at age 43 and died at age 78. Case 4 was a previously described female with a family history of PD caused by a heterozygous mutation in *SNCA* encoding G51D α-synuclein. She was diagnosed with PD at age 69 and developed cognitive impairment at age 71. Case 5 was an 87-year-old man with neuropathologically confirmed PD who died after an 8-year history of prominent resting tremor and bradykinesia. He developed dementia approximately 3 years after his PD diagnosis.

Extraction of α-synuclein filaments

Sarkosyl-insoluble material was extracted from fresh-frozen frontal cortex and putamen of individuals with MSA and MSA-FTLD, frontal cortex of individuals with PDD (G51D), PD (H50Q), and PDD (WT), essentially as described [41]. In brief, tissues were homogenized in 20 vol (v/w) extraction buffer consisting of 10 mM Tris-HCl, pH 7.5, 0.8 M NaCl, 20% sucrose and 1 mM EGTA. Homogenates were brought to 2% sarkosyl and incubated for 60 min at 37° C. Following a 10 min centrifugation at 10,000g, the supernatants were spun at 100,000g for 30 min. Sarkosyl-insoluble pellets were resuspended in 100 µl/g of elution buffer (20 mM Tris-HCl, pH 7.5, and 50mM NaCl) for further studies.

Binding of ACI-12589 to α-synuclein filaments

ACI-12589 was synthesized at AC Immune as described [34]. A 20mM solution was prepared using anhydrous dimethyl sulfoxide (DMSO) and stored at –20 ºC. α-synuclein filaments were extracted using the sarkosyl method from two cases and suspended in 100 µl/g elution buffer (20 mM Tris-HCl, pH 7.5, and 50mM NaCl), then were incubated with 20 µM ACI-12589 for 3.5-12 h at room temperature.

Electron cryo-microscopy

Extracted filaments were centrifuged at 3,000 g for 3 minutes and applied to glow-discharged holey carbon gold grids (Quantifoil Au R1.2/1.3, 300 mesh) and holey carbon grids (Quantifoil Cu R1.2/1.3, 300 mesh), which were glow-discharged with a Gatan Model 950 Advanced Plasma System using the carbon glow recipe for 30 s. Aliquots of 3 µl were applied to the grids and blotted with filter paper (Ted Pella 595 Filter Paper) at 100% humidity and 8 °C, and plunge-frozen in liquid ethane using an FEI Vitrobot Mark IV (Thermo Fisher Scientific). For MSA case 1 and case 2, datasets were acquired on Titan Krios G2 and G4 microscopes (Thermo Fisher Scientific) operated at 300 kV. For G51D, H50Q and WT cases, datasets were acquired on Titan Krios G3 microscopes (Thermo Fisher Scientific) operated at 300 kV. Images for the MSA case 1, G51D case, H50Q case and WT case were acquired using a Gatan K3 detector in super-resolution counting mode, using a Bio-quantum energy filter (Gatan) with a slit width of 20 eV. Images for MSA case 2 were acquired using a Falcon-4i detector (Thermo Fisher Scientific) in EER mode with a flux of 8 electrons/pixel/s and a Selectris-X energy filter (Thermo Fisher Scientific) with a slit width of 10 eV to remove inelastically scattered electrons. Images for MSA cases were recorded with a total dose of 40 electrons per $Å^{2.}$ The G51D case, H50Q case and WT case were recorded with a total dose of 50 electrons per $Å^2$. Further details can be found in Supplementary Table 2.

Helical reconstruction

Movie frames were gain-corrected, aligned, dose-weighted and then summed into a single micrograph using RELION's own motion correction program [42]. Contrast transfer function (CTF) parameters were estimated using CTFFIND-4.1 [43]. All subsequent image-

processing steps were performed using helical reconstruction methods in RELION [42, 44].Movie frames were gain-corrected, aligned, dose-weighted and then summed into a single micrograph using RELION's own motion correction program [42]. Contrast transfer function (CTF) parameters were estimated using CTFFIND-4.1 [43]. All subsequent image-processing steps were performed using helical reconstruction methods in RELION [42, 44]. α-synuclein filaments were picked manually (Extended Data Fig. 1). For all data sets, reference-free 2D classification was performed to select suitable segments for further processing. Initial 3D reference models were generated *de novo* from 2D class averages using an estimated rise of 4.75 Å and helical twists according to the observed cross-over distances of the filaments in the micrographs [45].

An initial model was generated using selected 2D class averages and a calculated crossover of 593 Å for type I filaments and 598 Å for type II filaments. G51D apo map model (EMD-70252) was used as initial model of G51D case, H50Q apo map model (EMD-70253) was used as initial model of H50Q case, and WT apo map model (EMD-15285) was used as initial model of WT case. Combinations of 3D auto-refinements and 3D classifications were used to select the best segments for each structure. For both data sets, Bayesian polishing[46] and CTF refinement [47] were performed to further increase the resolution of the reconstructions. Final reconstructions were sharpened using standard post-processing procedures in RELION, and overall final resolutions were estimated from Fourier shell correlations (FSCs) at 0.143 between the independently refined half-maps, using phase randomisation to correct for convolution effects of a generous, soft-edged solvent mask [48]. Using the relion_helix_toolbox program, helical symmetries were imposed on the post-processed maps, which were then used for model building and refinement. For further details, see Supplementary Table 2 and Fig. 1.

Difference map calculation with EMDA

To evaluate PET tracer or ligand-associated densities, difference maps were calculated using the EMDA [35]. Prior to subtraction, both cryo-EM reconstructions were resampled to the same pixel size and box dimensions to ensure grid compatibility. The maps were then aligned into a common coordinate frame by overlaying one reconstruction onto the other with *emda overlay --map*, which also provided an estimate of the relative displacement of

structural domains. Following alignment, difference maps were generated using the *emda diffmap* function with a resolution cutoff of 3.0 Å (--res 3). This procedure highlights local regions of positive and negative density corresponding to structural rearrangements or additional features between the two states.

Model building and refinement

Atomic models comprising one β-sheet rung were built in Coot [49] with the PDB models 6XYO for MSA type I, 6XYP for MSA type II filaments, and 9O9J for G51D. Coordinate refinements were performed using *Servalcat*[50]. Final models were obtained using refinement of all rungs with full occupancies of the ligand molecules against the half-maps in *Servalcat*. Additional information can be found in Supplementary Table 2.

Data availability

Cryo-EM maps were deposited to the EM Data Bank under accession codes EMD-78243, EMD-78904, and EMD-77417. Corresponding refined atomic models were deposited to the PDB under accession codes PDB: 37KR, 38LK, and 36EK. Please address requests for materials to the corresponding authors. Source data are provided with this paper.

Acknowledgements

We thank the patients and their families without whose generous donations this study would not have been possible. We thank the staff of the Queen Square Brain Bank for their help with material preparation. We thank AC-Immune for providing the PET tracer ACI-12589. The MSA Case1, G51D, H50Q and WT cases cryo-EM datasets were collected at the David Van Andel Advanced Cryo-Electron Microscopy Suite at the Van Andel Institute (Grand Rapids, MI). We thank the Van Andel Institute Cryo-EM Core (RRID:SCR_023210), especially Gongpu Zhao and Xing Meng for their assistance with data collection. We thank VAI High-performance computing team for their support. This work was funded by Van Andel Institute and a West Michigan Neuro-degenerative Diseases Program Pilot Award (MiP.017) to Y.Y.. It was also supported by the Japan Agency for Medical Research and Development (AMED; JP24wm0625120 to A.T. and JP24dk0207074h0001 to M.H.). We also thank Sjors H.W. Scheres and Michel Goedert for their advice and helpful discussions. We thank the Electron Microscopy Facility at the Medical Research Council Laboratory of Molecular Biology (MRC-LMB) for assistance with cryo-EM data collection for MSA case 2, and Jake Grimmett, Toby Darling and Ivan Clayson for support with high-performance computing. We are grateful to Paul Emsley, Rangana Warshamanage, Fei Long and Garib Murshudov for helpful discussions.

Author contributions

P.W.C., K.H., M.H., and Z.J. identified patients; H.H., and H.M. carried out genetic analysis; F.C. provided the compound; K.E., H.Z., A.T. and Y.Y. prepared filaments; K.E., H.Z., and Y.Y. performed cryo-EM data acquisition; K.E., H.Z., and Y.Y. performed cryo-EM structure determination and analysis; Y.Y. supervised the project; all authors contributed to writing the manuscript.

Competing interests

The authors declare no competing interests.

Supplementary Table 1 | Information of human cases.

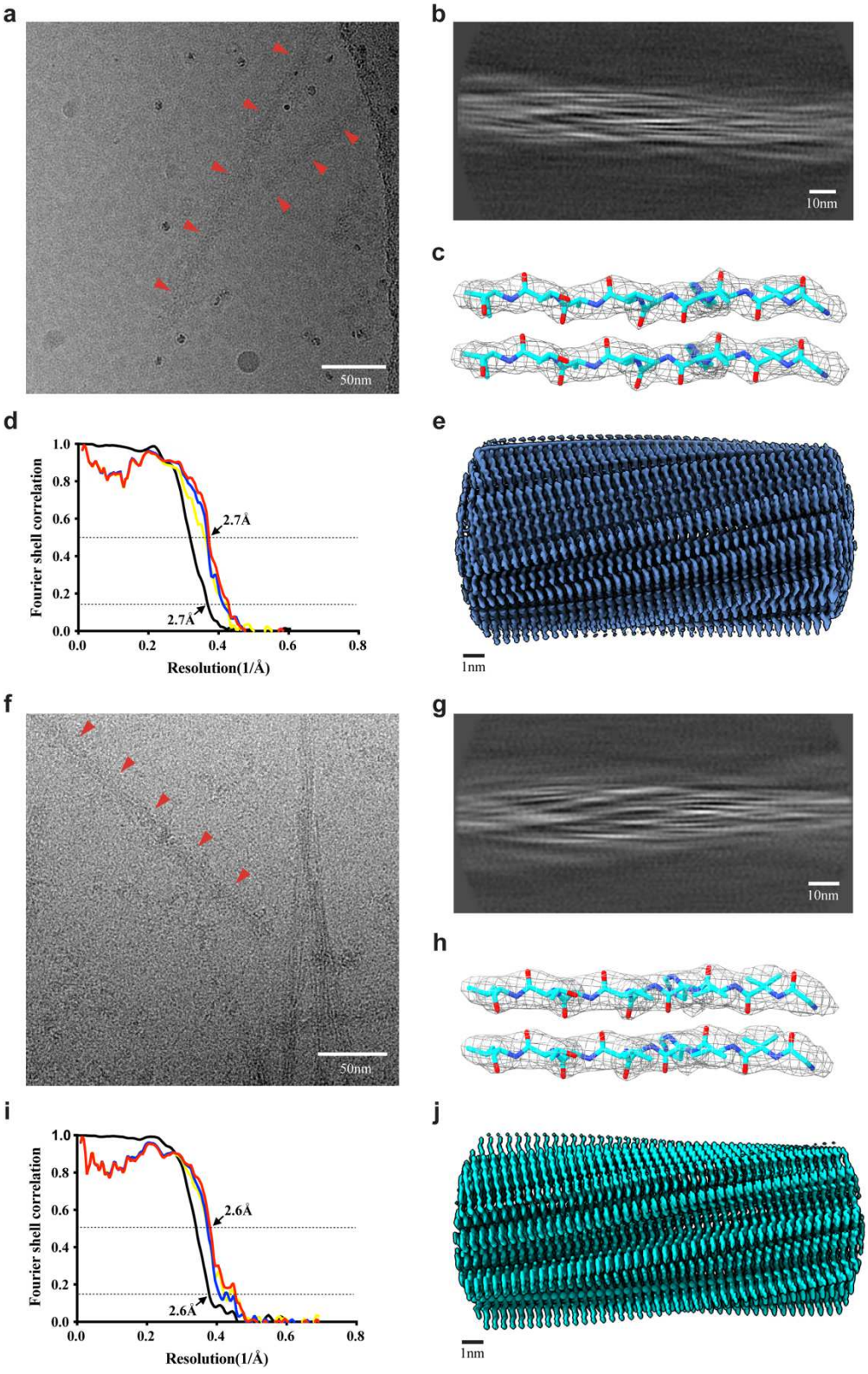
CASE	GENDER	AGE OF ONSET (YEARS)	AGE OF DEATH (YEARS)	DISEASE DURATION (YEARS)	CLINICOPATHOLOGICAL DIAGNOSIS
MSA CASE 1	Female	76	85	9	MSA
MSA CASE 2	Female	58	66	8	MSA-FTLD
G51D (HETEROZYGOUS)	Female	69	75	6	PDD
H50Q (HETEROZYGOUS)	Female	44	78	34	PD
WT	Male	79	87	8	PDD

Supplementary Table 2 | Cryo-EM data acquisition and structure determination.

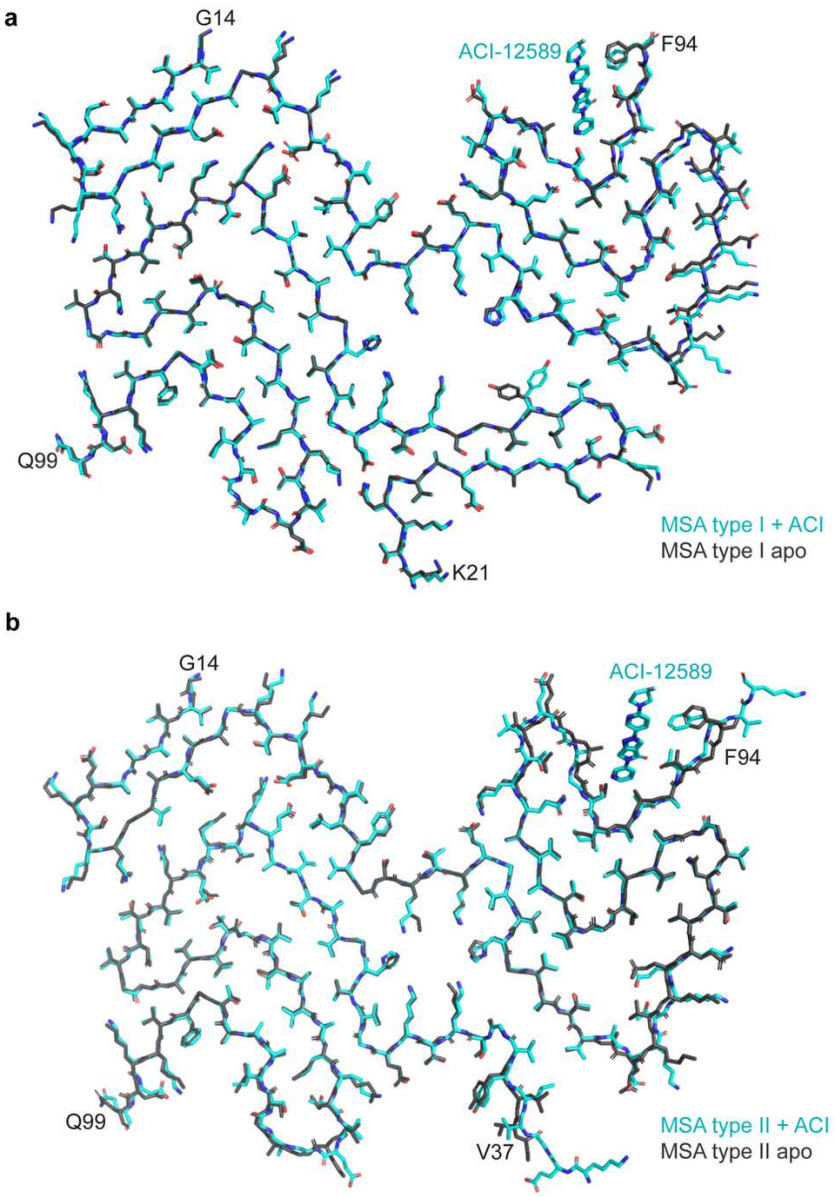
	MSA _ACI (CASE1, TYPE1)	MSA_ACI (CASE2, TYPE2)	G51D_ACI	H50Q (INCUBATION WITH ACI)	WT (INCUBATION WITH ACI)
PDB/EMDB	37KR/EMD-78243	38LK/EMD-78904	36EK/EMD-77417	EMD-79856	EMD-79855
DATA ACQUISITION					
ELECTRON GUN	Krios G2	Krios G4	Krios G3	Krios G3	Krios G3
DETECTOR	K3	Falcon4i	K3	K3	K3
ENERGY FILTER SLIT (EV)	20	10	20	20	20
MAGNIFICATION	96,000	165,000	105,000	105,000	105,000
VOLTAGE (KV)	300	300	300	300	300
ELECTRON DOSE ($E^{-}/Å^{2}$)	50	40	50	50	50
DEFOCUS RANGE (MM)	–1 to -2.4	–1 to -2.4	-1.2 to -1.8	-1.2 to -1.8	-1.2 to -2
PIXEL SIZE (Å)	0.828	0.723	0.828	0.86	0.926
MAP REFINEMENT					
SYMMETRY IMPOSED	C1	C1	C1	C1	C1
INITIAL PARTICLE IMAGES (NO.)	298,689	183,315	89,504	81,732	72,579

FINAL PARTICLE IMAGES (NO.)	112,655	54,932	23,486	55,512	65,000
MAP RESOLUTION (Å)	2.72	2.63	3.03	3.34	2.76
FSC THRESHOLD	0.143	0.143	0.143	0.143	0.143
HELICAL TWIST (°)	-1.41	-1.43	179.92	0.82	0.84
HELICAL RISE (Å)	4.73	4.73	2.39	4.98	4.77
MODEL REFINEMENT					
MODEL RESOLUTION (Å)	2.72	2.70	3.03		
FSC THRESHOLD	0.5	0.5	0.5		
MAP SHARPENING *B* FACTOR (Å^2)	-50	-50	-50		
MODEL COMPOSITION					
NON-HYDROGEN ATOMS	5700	6462	2685		
PROTEIN RESIDUES	800	894	395		
LIGANDS	5	6	0		
B FACTORS (Å^2)					
PROTEIN	61.9	72.7	68.2		
R.M.S. DEVIATIONS					
BOND LENGTHS (Å)	0.0084	0.0091	0.0093		
BOND ANGLES (°)	1.61	1.473	1.94		
VALIDATION					
MOLPROBITY SCORE	1.52	1.63	1.95		
CLASHSCORE	3.08	3.99	7.66		
POOR ROTAMERS (%)	0.93	0.98	0		
RAMACHANDRAN PLOT					
FAVORED (%)	93.59	93.10	90.67		
ALLOWED (%)	6.41	6.90	9.33		
DISALLOWED (%)	0	0	0		

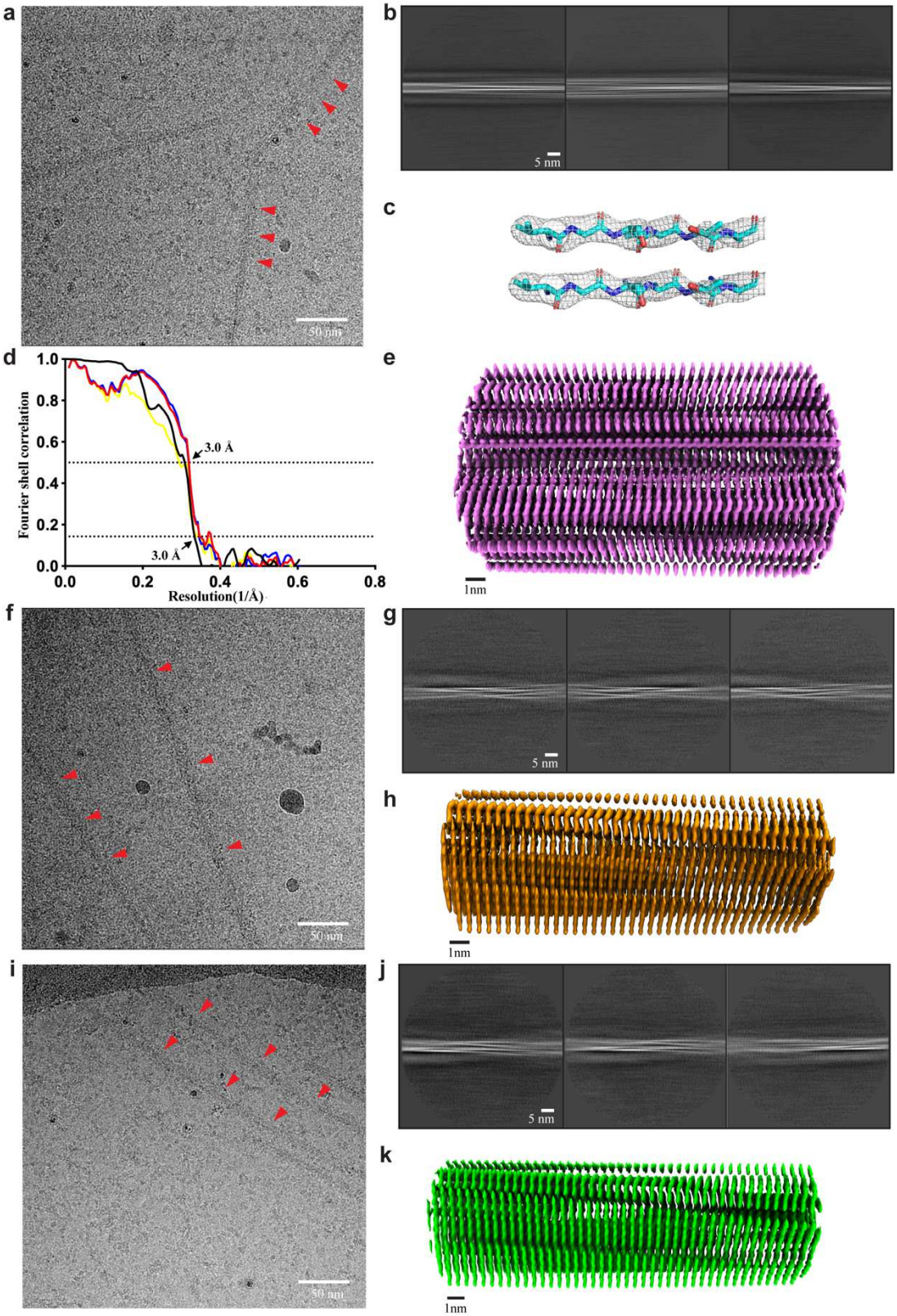
Extended Data Figures



Extended Data Fig. 1 | Cryo-EM images, maps, and resolution estimates. Images of α-synuclein filaments (red arrows) of MSA type I (**a**) and MSA type II (**f**) with ACI. Scale bars, 50 nm. Class 2D averages of MSA type I (**b**) and type II (**g**) filaments. Scale bars, 10 nm. Zoomed-in view of the main chain showing density of the oxygen atoms of MSA type I (**c**) and type II (**h**) filaments. **d** and **i,** Fourier shell correlation (FSC) curves for cryo-EM maps (d for MSA type I and i for MSA type II) are shown in black; for the final refined atomic model against the final cryo-EM map in red; for the atomic model refined in the first half map against that half map in blue; for the refined atomic model in the first half map against the other half map in yellow. Side view of the 3D reconstructions of MSA type I (**e**) and type II (**j**) filaments. Scale bars, 1 nm.

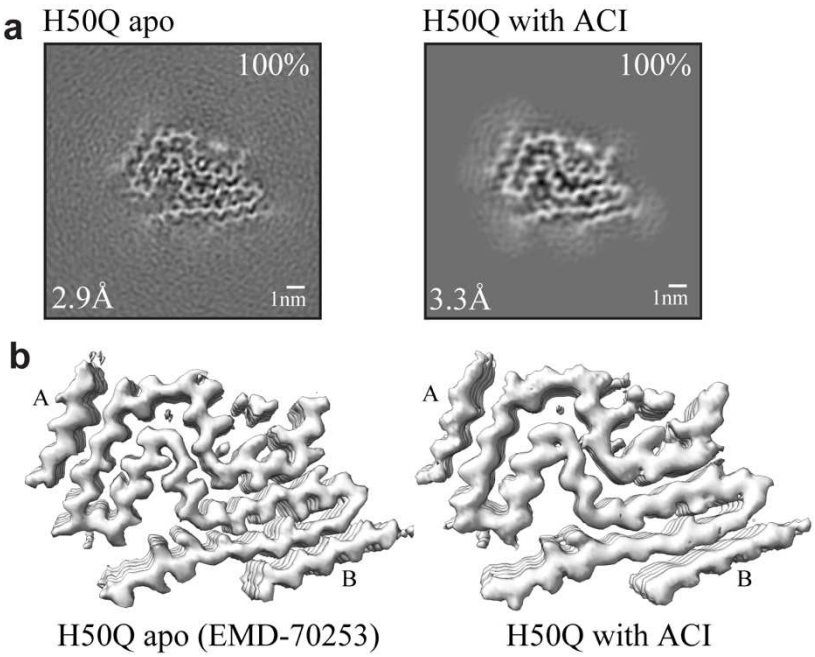


Extended Data Fig. 2 | Superposition of apo filament structures with ligand-bound structures. **a,** Superposition of MSA type I apo α-synuclein filament structure (PDB 6XYO) in magenta with the ligand-bound structure in cyan. **b,** Superposition of MSA type II apo α-synuclein filament structure (PDB 6XYP) in purple with the ligand-bound structure in cyan.

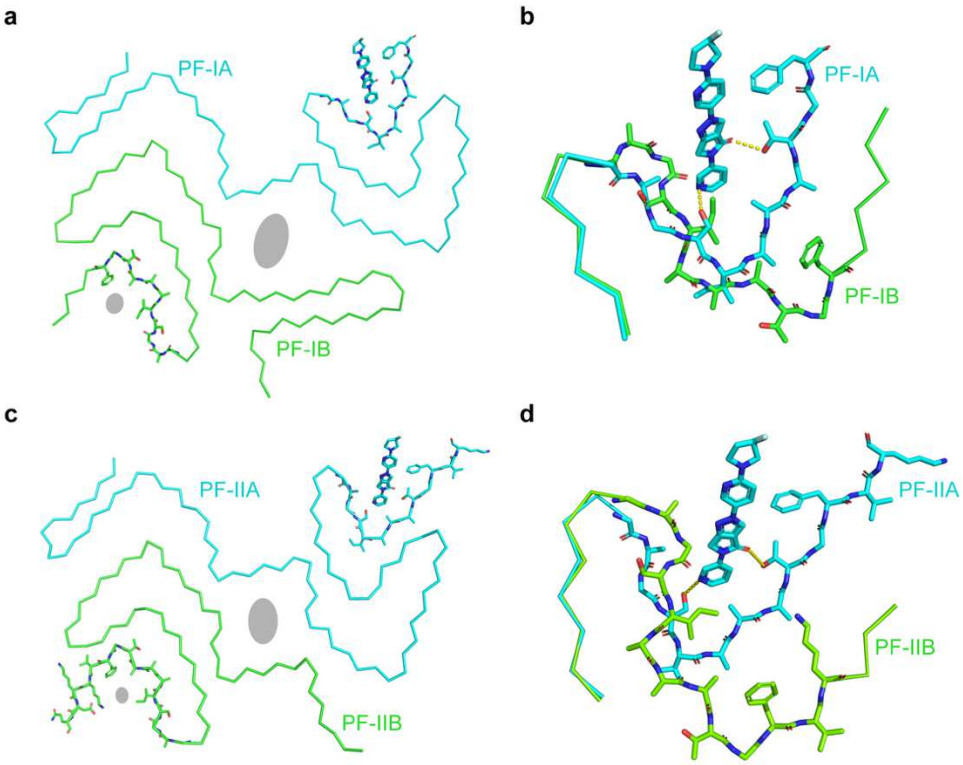


Extended Data Fig. 3 | Cryo-EM images, maps, and resolution estimates. **a, f** and **l,** Images of α-synuclein filaments (red arrows) of G51D, H50Q and WT with ACI. Scale

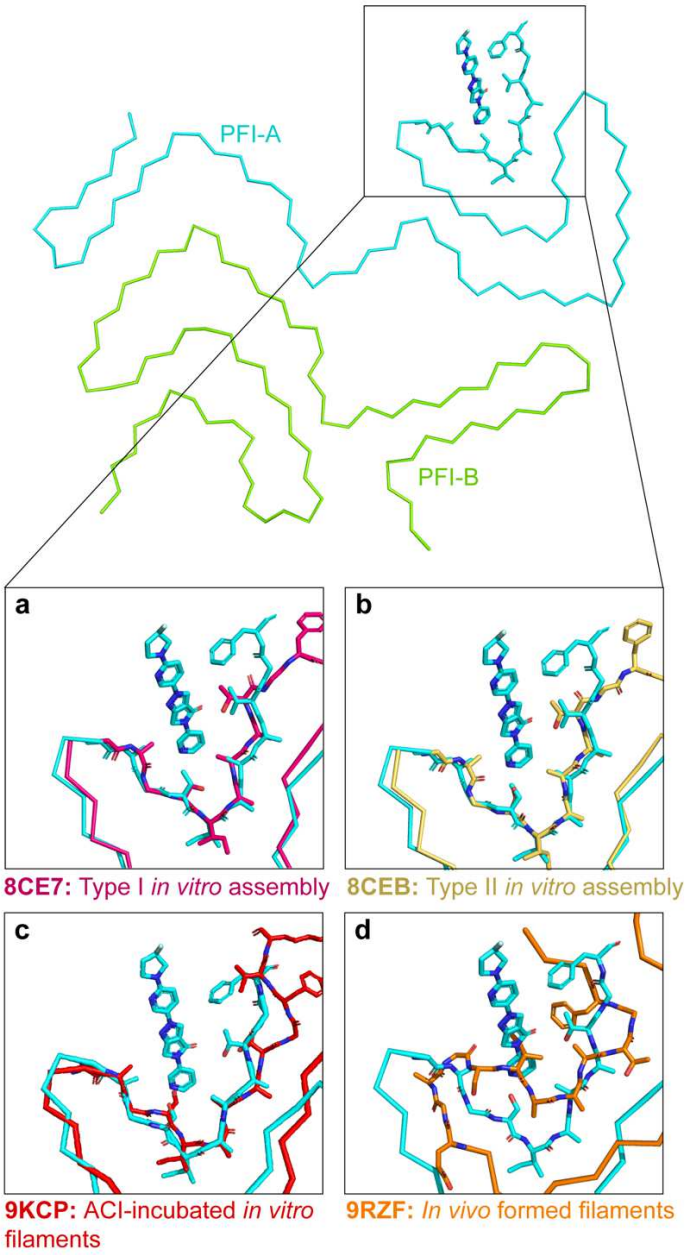
bars, 50 nm. **b, g** and **j,** Class 2D averages of G51D (b), H50Q (g) and WT (j) filaments. Scale bars, 5 nm. **c,** Zoomed-in view of the main chain showing density of the oxygen atoms of G51D filaments. **d,** Fourier shell correlation (FSC) curves for G51D cryo-EM maps are shown in black; for the final refined atomic model against the final cryo-EM map in red; for the atomic model refined in the first half map against that half map in blue; for the refined atomic model in the first half map against the other half map in yellow. **e, h** and **k,** Side view of the 3D reconstructions of G51D (e), H50Q (h) and WT (k) filaments.



Extended Data Fig. 4 | Cryo-EM maps of H50Q α-synuclein filaments with ACI-12589. **a,** Cryo-EM maps of H50Q filaments without and with ACI-12589 PET tracer. Scales, 1nm. **b,** Top view of cryo-EM maps of H50Q filaments without and with ACI-12589.



Extended Data Fig. 5 | ACI-12589 binds to protofilament A of MSA filaments. **a,** Atomic model of ACI-12589 bound to type I filament. Residues G84 – F94 are shown as sticks for protofilament IA (cyan) and protofilament IB (green). **b,** Superposition on C-terminus of protofilament IA and IB from MSA type I filament. Protofilament IA with ACI-12589 is in cyan, while protofilament IB in green. **c,** Atomic model of ACI-12589 bound to type II filaments. Residues G84-K96 are shown as sticks for protofilament IIA (cyan) and protofilament IIB (green). **d,** Superposition on C-terminus of protofilament IIA and IIB from MSA type II filament. Protofilament IIA with ACI-12589 is in cyan, while protofilament IIB in green. Hydrogen bonds are shown in yellow.



Extended Data Fig. 6 | Superposition of type I MSA protofilament A (cyan) with representative α-synuclein filament structures. **a,** Type I in vitro assembly generated from wild-type and mutant α-synuclein (PDB: 8CE7, magenta). **b,** Type II in vitro assembly generated from wild-type and mutant α-synuclein (PDB: 8CEB, yellow). **c,** ACI-bound polymorph 6A6B (PDB: 9KCP, red). **d,** In vivo-formed filaments purified from the brain of an M83+/- mouse following injection with recombinant α-synuclein filaments (PDB: 9RZF, orange).

References

1. Spillantini MG, Schmidt ML, Lee VM, Trojanowski JQ, Jakes R, Goedert M. Alpha-synuclein in Lewy bodies. Nature. 1997;388(6645):839-40. doi: 10.1038/42166. PubMed PMID: 9278044.
2. Iwatsubo T. [Parkinson's disease, dementia with Lewy bodies, multiple system atrophy and alpha-synuclein]. Rinsho Shinkeigaku. 1999;39(12):1285-6. PubMed PMID: 10791099.
3. Jellinger KA. Multiple System Atrophy: An Oligodendroglioneural Synucleinopathy1. J Alzheimers Dis. 2018;62(3):1141-79. doi: 10.3233/JAD-170397. PubMed PMID: 28984582; PMCID: PMC5870010.
4. Sidoroff V, Bower P, Stefanova N, Fanciulli A, Stankovic I, Poewe W, Seppi K, Wenning GK, Krismer F. Disease-Modifying Therapies for Multiple System Atrophy: Where Are We in 2022? J Parkinsons Dis. 2022;12(5):1369-87. doi: 10.3233/JPD-223183. PubMed PMID: 35491799; PMCID: PMC9398078.
5. Arias-Carrion O, Guerra-Crespo M, Padilla-Godinez FJ, Soto-Rojas LO, Manjarrez E. alpha-Synuclein Pathology in Synucleinopathies: Mechanisms, Biomarkers, and Therapeutic Challenges. Int J Mol Sci. 2025;26(11). Epub 20250604. doi: 10.3390/ijms26115405. PubMed PMID: 40508212; PMCID: PMC12155115.
6. Ayers JI, Lee J, Monteiro O, Woerman AL, Lazar AA, Condello C, Paras NA, Prusiner SB. Different alpha-synuclein prion strains cause dementia with Lewy bodies and multiple system atrophy. Proc Natl Acad Sci U S A. 2022;119(6). doi: 10.1073/pnas.2113489119. PubMed PMID: 35115402; PMCID: PMC8833220.
7. Yang Y, Shi Y, Schweighauser M, Zhang X, Kotecha A, Murzin AG, Garringer HJ, Cullinane PW, Saito Y, Foroud T, Warner TT, Hasegawa K, Vidal R, Murayama S, Revesz T, Ghetti B, Hasegawa M, Lashley T, Scheres SHW, Goedert M. Structures of alpha-synuclein filaments from human brains with Lewy pathology. Nature. 2022;610(7933):791-5. Epub 20220915. doi: 10.1038/s41586-022-05319-3. PubMed PMID: 36108674; PMCID: PMC7613749.
8. Yan NL, Mayer M, Melo AA, Ayers JI, Mordes DA, Seeley WW, Prusiner SB, Tse E, Chittoor-Vinod VG, Merz GE. Cryo-EM Structures of Infectious Low-Twist alpha-Synuclein Filaments in Lewy Bodies. bioRxiv. 2026. Epub 20260917. doi: 10.64898/2026.09.16.752119. PubMed PMID: 42780058; PMCID: PMC13596415.
9. Zhang H, Murzin AG, Macdonald JA, Hinton TV, Peak-Chew S, Franco C, Cullinane PW, Warner T, Okuzumi A, Real R, Nishioka K, Taniguchi D, Kaneda D, Morris H, Houlden H, Ghetti B, Hattori N, Jaunmuktane Z, Yang Y, Scheres SHW, Goedert M. Dimerisation and twist reversal of the Lewy fold in α-synuclein mutants with Parkinson’s disease and dementia. bioRxiv. 2026:2026.04.07.716933. doi: 10.64898/2026.04.07.716933.
10. Lesage S, Anheim M, Letournel F, Bousset L, Honore A, Rozas N, Pieri L, Madiona K, Durr A, Melki R, Verny C, Brice A, French Parkinson's Disease Genetics Study G. G51D alpha-synuclein mutation causes a novel parkinsonian-pyramidal syndrome. Ann Neurol. 2013;73(4):459-71. doi: 10.1002/ana.23894. PubMed PMID: 23526723.
11. Kiely AP, Ling H, Asi YT, Kara E, Proukakis C, Schapira AH, Morris HR, Roberts HC, Lubbe S, Limousin P, Lewis PA, Lees AJ, Quinn N, Hardy J, Love S, Revesz T, Houlden H,

Holton JL. Distinct clinical and neuropathological features of G51D SNCA mutation cases compared with SNCA duplication and H50Q mutation. Mol Neurodegener. 2015;10:41. Epub 20150827. doi: 10.1186/s13024-015-0038-3. PubMed PMID: 26306801; PMCID: PMC4549856.
12. Khalaf O, Fauvet B, Oueslati A, Dikiy I, Mahul-Mellier AL, Ruggeri FS, Mbefo MK, Vercruysse F, Dietler G, Lee SJ, Eliezer D, Lashuel HA. The H50Q mutation enhances alpha-synuclein aggregation, secretion, and toxicity. J Biol Chem. 2014;289(32):21856-76. Epub 20140616. doi: 10.1074/jbc.M114.553297. PubMed PMID: 24936070; PMCID: PMC4139205.
13. Schweighauser M, Shi Y, Tarutani A, Kametani F, Murzin AG, Ghetti B, Matsubara T, Tomita T, Ando T, Hasegawa K, Murayama S, Yoshida M, Hasegawa M, Scheres SHW, Goedert M. Structures of alpha-synuclein filaments from multiple system atrophy. Nature. 2020;585(7825):464-9. Epub 20200527. doi: 10.1038/s41586-020-2317-6. PubMed PMID: 32461689; PMCID: PMC7116528.
14. Yan NL, Candido F, Tse E, Melo AA, Prusiner SB, Mordes DA, Southworth DR, Paras NA, Merz GE. Cryo-EM structure of a novel alpha-synuclein filament subtype from multiple system atrophy. FEBS Lett. 2025;599(1):33-40. Epub 20241107. doi: 10.1002/1873-3468.15048. PubMed PMID: 39511911; PMCID: PMC11726156.
15. Bao W, Xie F, Zuo C, Guan Y, Huang YH. PET Neuroimaging of Alzheimer's Disease: Radiotracers and Their Utility in Clinical Research. Front Aging Neurosci. 2021;13:624330. Epub 20210506. doi: 10.3389/fnagi.2021.624330. PubMed PMID: 34025386; PMCID: PMC8134674.
16. Wang L, Bharti, Kumar R, Pavlov PF, Winblad B. Small molecule therapeutics for tauopathy in Alzheimer's disease: Walking on the path of most resistance. Eur J Med Chem. 2021;209:112915. Epub 20201015. doi: 10.1016/j.ejmech.2020.112915. PubMed PMID: 33139110.
17. Maschio C, Ni R. Amyloid and Tau Positron Emission Tomography Imaging in Alzheimer's Disease and Other Tauopathies. Front Aging Neurosci. 2022;14:838034. Epub 20220422. doi: 10.3389/fnagi.2022.838034. PubMed PMID: 35527737; PMCID: PMC9074832.
18. Wang J, Jin C, Zhou J, Zhou R, Tian M, Lee HJ, Zhang H. PET molecular imaging for pathophysiological visualization in Alzheimer's disease. Eur J Nucl Med Mol Imaging. 2023;50(3):765-83. Epub 20221114. doi: 10.1007/s00259-022-05999-z. PubMed PMID: 36372804; PMCID: PMC9852140.
19. Heurling K, Leuzy A, Zimmer ER, Lubberink M, Nordberg A. Imaging beta-amyloid using [(18)F]flutemetamol positron emission tomography: from dosimetry to clinical diagnosis. Eur J Nucl Med Mol Imaging. 2016;43(2):362-73. Epub 20151006. doi: 10.1007/s00259-015-3208-1. PubMed PMID: 26440450.
20. Han EJ, Sung YE, Jung MH, O JH, Youn JC. 18 F-Flutemetamol PET/CT for Transthyretin Amyloid Cardiomyopathy : Timing Matters. Clin Nucl Med. 2022;47(12):1074-6. Epub 20221014. doi: 10.1097/RLU.0000000000004411. PubMed PMID: 36240762.
21. Romoli M, Marinoni G, Tagliabue L, Capozza A, Matteucci F, Mattone V, Longoni M, Cenni P, Ruggiero M, Rifino N, Canavero I, Boncoraglio G, Stanziano M, Bersano A, Storti B. (18F)Flutemetamol-PET Aided Classification of Cerebral Amyloid Angiopathy: A Multicenter

Study. Neurology. 2024;103(4):e209719. Epub 20240731. doi: 10.1212/WNL.0000000000209719. PubMed PMID: 39083717.
22. Xiang J, Tao Y, Xia Y, Luo S, Zhao Q, Li B, Zhang X, Sun Y, Xia W, Zhang M, Kang SS, Ahn EH, Liu X, Xie F, Guan Y, Yang JJ, Bu L, Wu S, Wang X, Cao X, Liu C, Zhang Z, Li D, Ye K. Development of an alpha-synuclein positron emission tomography tracer for imaging synucleinopathies. Cell. 2023;186(16):3350-67 e19. Epub 20230707. doi: 10.1016/j.cell.2023.06.004. PubMed PMID: 37421950; PMCID: PMC10527432.
23. Tao Y, Xia W, Zhao Q, Xiang H, Han C, Zhang S, Gu W, Tang W, Li Y, Tan L, Li D, Liu C. Structural mechanism for specific binding of chemical compounds to amyloid fibrils. Nat Chem Biol. 2023;19(10):1235-45. Epub 20230703. doi: 10.1038/s41589-023-01370-x. PubMed PMID: 37400537.
24. Seidler PM, Murray KA, Boyer DR, Ge P, Sawaya MR, Hu CJ, Cheng X, Abskharon R, Pan H, DeTure MA, Williams CK, Dickson DW, Vinters HV, Eisenberg DS. Structure-based discovery of small molecules that disaggregate Alzheimer's disease tissue derived tau fibrils in vitro. Nature communications. 2022;13(1):5451. Epub 20220916. doi: 10.1038/s41467-022-32951-4. PubMed PMID: 36114178; PMCID: PMC9481533.
25. Li X, Bi L, Zhang S, Xu Q, Xia W, Tao Y, Wu S, Li Y, Le W, Kang W, Li D, Sun B, Liu C. Single-Molecule Insight Into alpha-Synuclein Fibril Structure and Mechanics Modulated by Chemical Compounds. Adv Sci (Weinh). 2025;12(14):e2416721. Epub 20250214. doi: 10.1002/advs.202416721. PubMed PMID: 39951335; PMCID: PMC11984887.
26. Shi Y, Murzin AG, Falcon B, Epstein A, Machin J, Tempest P, Newell KL, Vidal R, Garringer HJ, Sahara N, Higuchi M, Ghetti B, Jang MK, Scheres SHW, Goedert M. Cryo-EM structures of tau filaments from Alzheimer's disease with PET ligand APN-1607. Acta Neuropathol. 2021;141(5):697-708. Epub 20210316. doi: 10.1007/s00401-021-02294-3. PubMed PMID: 33723967; PMCID: PMC8043864.
27. Merz GE, Chalkley MJ, Tan SK, Tse E, Lee J, Prusiner SB, Paras NA, DeGrado WF, Southworth DR. Stacked binding of a PET ligand to Alzheimer's tau paired helical filaments. Nature communications. 2023;14(1):3048. Epub 20230526. doi: 10.1038/s41467-023-38537-y. PubMed PMID: 37236970; PMCID: PMC10220082.
28. Kunach P, Vaquer-Alicea J, Smith MS, Monistrol J, Hopewell R, Moquin L, Therriault J, Tissot C, Rahmouni N, Massarweh G, Soucy JP, Guiot MC, Shoichet BK, Rosa-Neto P, Diamond MI, Shahmoradian SH. Cryo-EM structure of Alzheimer's disease tau filaments with PET ligand MK-6240. Nature communications. 2024;15(1):8497. Epub 20241001. doi: 10.1038/s41467-024-52265-x. PubMed PMID: 39353896; PMCID: PMC11445244.
29. Shi Y, Ghetti B, Goedert M, Scheres SHW. Cryo-EM Structures of Chronic Traumatic Encephalopathy Tau Filaments with PET Ligand Flortaucipir. J Mol Biol. 2023;435(11):168025. Epub 20230616. doi: 10.1016/j.jmb.2023.168025. PubMed PMID: 37330290; PMCID: PMC7615338.
30. Liu K, Tao Y, Zhao Q, Xia W, Li X, Zhang S, Yao Y, Xiang H, Han C, Tan L, Sun B, Li D, Li A, Liu C. Binding adaptability of chemical ligands to polymorphic alpha-synuclein amyloid fibrils. Proc Natl Acad Sci U S A. 2024;121(35):e2321633121. Epub 20240822. doi: 10.1073/pnas.2321633121. PubMed PMID: 39172784; PMCID: PMC11363296.
31. Zhao Q, Fan Y, Zhao W, Ni Y, Tao Y, Bian J, Xia W, Yu W, Fan Z, Liu C, Sun B, Le W, Li W, Wang J, Li D. A Tau PET tracer PBB3 binds to TMEM106B amyloid fibril in brain. Cell Discov.

2024;10(1):50. Epub 20240514. doi: 10.1038/s41421-024-00674-z. PubMed PMID: 38744856; PMCID: PMC11094151.
32. Saw RS, Haas S, Schmidt F, Ryazanov S, Leonov A, Bleher D, Grotegerd AK, Kuebler L, Roeben B, Schmidt F, Reimold M, Bonanno F, Ruf VC, Dahl B, Sandiego CM, Henry KE, Papadopoulos I, Schaller M, Kahle PJ, Levin J, Gasser T, Brockmann K, Reischl G, la Fougere C, Pichler BJ, Maurer A, Griesinger C, Giese A, Herfert K. The PET tracer [(11)C]MODAG-005 targets alpha-synuclein aggregates in the brain. Sci Transl Med. 2026;18(851):eaec0813. Epub 20260527. doi: 10.1126/scitranslmed.aec0813. PubMed PMID: 42202047.
33. Pees A, Grotegerd AK, Bleher D, Herfert K, Vasdev N. PET imaging of alpha-synuclein: from radiotracer design through in vitro and in vivo translation. Eur J Nucl Med Mol Imaging. 2026;53(6):4211-39. Epub 20260121. doi: 10.1007/s00259-025-07695-0. PubMed PMID: 41559331; PMCID: PMC13121216.
34. Smith R, Capotosti F, Schain M, Ohlsson T, Vokali E, Molette J, Touilloux T, Hliva V, Dimitrakopoulos IK, Puschmann A, Jogi J, Svenningsson P, Andreasson M, Sandiego C, Russell DS, Miranda-Azpiazu P, Halldin C, Stomrud E, Hall S, Bratteby K, Tampio L'Estrade E, Luthi-Carter R, Pfeifer A, Kosco-Vilbois M, Streffer J, Hansson O. The alpha-synuclein PET tracer [18F] ACI-12589 distinguishes multiple system atrophy from other neurodegenerative diseases. Nature communications. 2023;14(1):6750. Epub 20231027. doi: 10.1038/s41467-023-42305-3. PubMed PMID: 37891183; PMCID: PMC10611796.
35. Warshamanage R, Yamashita K, Murshudov GN. EMDA: A Python package for Electron Microscopy Data Analysis. J Struct Biol. 2022;214(1):107826. Epub 20211213. doi: 10.1016/j.jsb.2021.107826. PubMed PMID: 34915128; PMCID: PMC8935390.
36. Huettemann P, Mahadevan P, Lempart J, Tse E, Dehury B, Edwards BFP, Southworth DR, Sahoo BR, Jakob U. Amyloid accelerator polyphosphate fits as the mystery density in alpha-synuclein fibrils. PLoS Biol. 2024;22(10):e3002650. Epub 20241031. doi: 10.1371/journal.pbio.3002650. PubMed PMID: 39480879; PMCID: PMC11527176.
37. Murray KA, Hu CJ, Pan H, Lu J, Abskharon R, Bowler JT, Rosenberg GM, Williams CK, Elezi G, Balbirnie M, Faull KF, Vinters HV, Seidler PM, Eisenberg DS. Small molecules disaggregate alpha-synuclein and prevent seeding from patient brain-derived fibrils. Proc Natl Acad Sci U S A. 2023;120(7):e2217835120. Epub 20230209. doi: 10.1073/pnas.2217835120. PubMed PMID: 36757890; PMCID: PMC9963379.
38. Varlow C, Pees A, Stehouwer JS, Grotegerd AK, Bleher D, Guarino DS, Lindberg A, Tong J, Lopresti BJ, Knight AC, Zabrocki M, Nasser A, Shalgunov V, Ferri E, Cannazza G, McQuade P, Mathis CA, Mach RH, Battisti UM, Herfert K, Herth MM, Knudsen GM, Vasdev N. Autoradiography and preclinical PET studies with radiolabeled asyn-44 and ACI-12589 for imaging alpha-synuclein. J Parkinsons Dis. 2026;16(4):683-98. Epub 20260417. doi: 10.1177/1877718X261431108. PubMed PMID: 41995458; PMCID: PMC13224086.
39. Burger D, Kashyrina M, van den Heuvel L, de La Seigliere H, Lewis AJ, De Nuccio F, Mohammed I, Verchere J, Feuillie C, Berbon M, Arotcarena ML, Retailleau A, Bezard E, Canron MH, Meissner WG, Loquet A, Bousset L, Poujol C, Nilsson KPR, Laferriere F, Baron T, Lofrumento DD, De Giorgi F, Stahlberg H, Ichas F. Synthetic alpha-synuclein fibrils replicate in mice causing MSA-like pathology. Nature. 2025;648(8093):409-17. Epub 20251105. doi: 10.1038/s41586-025-09698-1. PubMed PMID: 41193804; PMCID: PMC12695662.

40. Balana AT, Mahul-Mellier AL, Nguyen BA, Horvath M, Javed A, Hard ER, Jasiqi Y, Singh P, Afrin S, Pedretti R, Singh V, Lee VM, Luk KC, Saelices L, Lashuel HA, Pratt MR. O-GlcNAc forces an alpha-synuclein amyloid strain with notably diminished seeding and pathology. Nat Chem Biol. 2024;20(5):646-55. Epub 20240212. doi: 10.1038/s41589-024-01551-2. PubMed PMID: 38347213; PMCID: PMC11062923.
41. Cullinane PW, Yang Y, Chelban V, Goh YY, Ebanks K, Curless T, Wrigley S, de Pablo-Fernandez E, Holton J, Peak-Chew S, Franco C, Woerman AL, Houlden H, Warner TT, Scheres SHW, Goedert M, Jaunmuktane Z. Identical Seeding Characteristics and Cryo-EM Filament Structures in FTLD-Synuclein and Typical Multiple System Atrophy. Neuropathol Appl Neurobiol. 2025;51(2):e70013. doi: 10.1111/nan.70013. PubMed PMID: 40135351; PMCID: PMC11937994.
42. He S, Scheres SHW. Helical reconstruction in RELION. J Struct Biol. 2017;198(3):163-76. Epub 2017/02/15. doi: 10.1016/j.jsb.2017.02.003. PubMed PMID: 28193500; PMCID: PMC5479445.
43. Rohou A, Grigorieff N. CTFFIND4: Fast and accurate defocus estimation from electron micrographs. J Struct Biol. 2015;192(2):216-21. Epub 20150813. doi: 10.1016/j.jsb.2015.08.008. PubMed PMID: 26278980; PMCID: PMC6760662.
44. Zivanov J, Nakane T, Forsberg BO, Kimanius D, Hagen WJ, Lindahl E, Scheres SH. New tools for automated high-resolution cryo-EM structure determination in RELION-3. Elife. 2018;7. Epub 20181109. doi: 10.7554/eLife.42166. PubMed PMID: 30412051; PMCID: PMC6250425.
45. Scheres SHW. Amyloid structure determination in RELION-3.1. Acta Crystallogr D Struct Biol. 2020;76(Pt 2):94-101. Epub 20200130. doi: 10.1107/S2059798319016577. PubMed PMID: 32038040; PMCID: PMC7008511.
46. Zivanov J, Nakane T, Scheres SHW. A Bayesian approach to beam-induced motion correction in cryo-EM single-particle analysis. IUCrJ. 2019;6(Pt 1):5-17. Epub 2019/02/05. doi: 10.1107/S205225251801463X. PubMed PMID: 30713699; PMCID: PMC6327179.
47. Zivanov J, Nakane T, Scheres SHW. Estimation of high-order aberrations and anisotropic magnification from cryo-EM data sets in RELION-3.1. IUCrJ. 2020;7(Pt 2):253-67. Epub 20200211. doi: 10.1107/S2052252520000081. PubMed PMID: 32148853; PMCID: PMC7055373.
48. Chen VB, Arendall WB, 3rd, Headd JJ, Keedy DA, Immormino RM, Kapral GJ, Murray LW, Richardson JS, Richardson DC. MolProbity: all-atom structure validation for macromolecular crystallography. Acta Crystallogr D Biol Crystallogr. 2010;66(Pt 1):12-21. Epub 20091221. doi: 10.1107/S0907444909042073. PubMed PMID: 20057044; PMCID: PMC2803126.
49. Emsley P, Lohkamp B, Scott WG, Cowtan K. Features and development ofCoot. Acta Crystallographica Section D Biological Crystallography. 2010;66(4):486-501. doi: 10.1107/s0907444910007493.
50. Yamashita K, Palmer CM, Burnley T, Murshudov GN. Cryo-EM single-particle structure refinement and map calculation using Servalcat. Acta Crystallogr D Struct Biol. 2021;77(Pt 10):1282-91. Epub 20210929. doi: 10.1107/S2059798321009475. PubMed PMID: 34605431; PMCID: PMC8489229.

Supplementary Files

This is a list of supplementary files associated with this preprint. Click to download.

- 4513ACIvalidationreport.pdf
- validationreportWTACI.pdf
- validationreportH50QACI.pdf
- validationreportG51DACI.pdf
- 9633ACIvalidationreport.pdf
- Archive.zip